

# Accurate and Real-Time Pedestrian Classification Based on UWB Doppler Radar Images and Their Radial Velocity Features

Kenshi SAHO<sup>†a)</sup>, Takuya SAKAMOTO<sup>†</sup>, *Members*, Toru SATO<sup>†</sup>, *Fellow*, Kenichi INOUE<sup>††</sup>, and Takeshi FUKUDA<sup>††</sup>, *Members*

**SUMMARY** The classification of human motion is an important aspect of monitoring pedestrian traffic. This requires the development of advanced surveillance and monitoring systems. Methods to achieve this have been proposed using micro-Doppler radars. However, reliable long-term data and/or complicated procedures are needed to classify motion accurately with these conventional methods because their accuracy and real-time capabilities are invariably inadequate. This paper proposes an accurate and real-time method for classifying the movements of pedestrians using ultra wide-band (UWB) Doppler radar to overcome these problems. The classification of various movements is achieved by extracting feature parameters based on UWB Doppler radar images and their radial velocity distributions. Experiments were carried out assuming six types of pedestrian movements (pedestrians swinging both arms, swinging only one arm, swinging no arms, on crutches, pushing wheelchairs, and seated in wheelchairs). We found they could be classified using the proposed feature parameters and a  $k$ -nearest neighbor algorithm. A classification accuracy of 96% was achieved with a mean calculation time of 0.55 s. Moreover, the classification accuracy was 99% using our proposed method for classifying three groups of pedestrian movements (normal walkers, those on crutches, and those in wheelchairs).

**key words:** human imaging, pedestrian classification, UWB Doppler radar, radial velocity distribution,  $k$ -nearest neighbor

## 1. Introduction

Using radar to identify people has great potential for surveillance and monitoring systems in towns, houses, shops, and hospitals. Many radar localization and imaging methods have been proposed and applied to detect the human body [1]–[5]. However, most of these methods need large antenna arrays or many radars placed at various locations and, therefore, the size and cost of the system have increased.

Studies to accomplish low-complexity radar systems have been conducted to develop methods of identifying and classifying targets using micro-Doppler radar [6]–[12]. These conventional methods are used to classify motion based on time-frequency micro-Doppler signatures. Kim and Ling proposed [6] a method of classifying human activities (e.g., walking, running, and sitting) using the parameters of a time-frequency distribution (e.g., offset, peak-to-peak value, and period), and they applied a support vector

machine (SVM). However, their method was not sufficiently accurate for practical use because it assumed motion would demonstrate clear differences in terms of its time-frequency distributions. Methods of processing time-frequency distributions have been proposed [7], [8] to classify three types of human gait: free arm-motion (FAM), which is characterized by swinging both arms, partial arm-motion (PAM), by swinging only one arm, and no arm-motion (NAM), by no motion in either arm. However, reliable and long-term data (at least 2 s duration) are needed to classify motion accurately using these methods. Although other micro-Doppler based methods of detecting targets and classifying motion have been proposed [9]–[12], they involve long-term data and/or complicated procedures, and their real-time capabilities and accuracy have been inadequate.

Ultra wide-band (UWB) radar is a powerful tool for solving these problems because of its high-resolution capability. A method of classifying human activities based on the waveform of UWB radar and principal component analysis has been proposed [13]. However, its accuracy in classification is insufficient because it only uses waveform information. An approach that uses shape information has been considered to achieve more accurate classification. We have already proposed a method of imaging humans using UWB Doppler radar interferometry [14]–[16], which provides high-resolution images of multiple scattering centers using a micro-Doppler radar technique and UWB signals. Furthermore, we proposed a method for rejecting false images caused by interference, and achieved reliable and real-time pedestrian imaging in a realistic environment [14]. Moreover, we confirmed features of walking motion with the radial velocity information of the estimated images [16]. However, to date we have not considered the classification of targets using UWB Doppler radar images.

In this paper, we present an accurate and real-time method of classifying pedestrians based on UWB Doppler radar images and their radial velocity features. We considered classifying three groups of pedestrians mainly in a hospital monitoring environment: a normal pedestrian group, a group on crutches, and a group in wheelchairs. We also considered classifying the types of pedestrians in more detail. Three types of human gait for the normal pedestrian group were assumed: those who swung their arms (FAM), those who held a bag with one hand (corresponding to PAM), and those who did not swing their arms (NAM). The target group in wheelchairs was composed of two types: a pedes-

Manuscript received January 17, 2013.

Manuscript revised May 17, 2013.

<sup>†</sup>The authors are with the Department of Communications and Computer Engineering, Graduate School of Informatics, Kyoto University, Kyoto-shi, 606-8501 Japan.

<sup>††</sup>The authors are with the Advanced Technology Research Laboratories, Panasonic Corporation, Kyoto-fu, 619-0237 Japan.

a) E-mail: ksaho@sato-lab.0t0.jp

DOI: 10.1587/transcom.E96.B.2563

trian pushing a person in a wheelchair and a person propping him/herself in a wheelchair. This study dealt with classifying these three groups and six types of pedestrian targets. We experimentally obtained results from imaging these types of pedestrians using UWB Doppler radar, and discuss the features of all the acquired images of the pedestrians. We also propose feature parameters extracted from the estimated images and their radial velocity distributions, and describe a method of classification using these parameters and a  $k$ -nearest neighbor ( $k$ -NN) algorithm, which is a powerful nonparametric technique for classifying patterns [17], [18]. The results revealed that we could accurately classify three groups and six types of pedestrians in real-time with our proposed classification method.

## 2. UWB Doppler Radar Imaging Method

### 2.1 System Configuration

Figure 1 shows a schematic of the setup for the UWB Doppler radar. We assume that the target is a single person walking toward the radar. A transmitting antenna Tx and receiving antennas Rx<sub>1</sub>, Rx<sub>2</sub>, and Rx<sub>3</sub> are set up on the  $y = 0$  plane. The positions of antennas Tx, Rx<sub>1</sub>, Rx<sub>2</sub>, and Rx<sub>3</sub> are expressed as  $(x, z) = (d/2, d/2+z_c), (-d/2, -d/2+z_c), (d/2, -d/2+z_c),$  and  $(-d/2, d/2+z_c)$ . The pair of receiving antennas Rx<sub>1</sub> and Rx<sub>2</sub> forms a horizontal interferometer and the pair Rx<sub>1</sub> and Rx<sub>3</sub> forms a vertical interferometer. Measurements are conducted in several antenna positions to acquire an image of the whole body and the imaging results are acquired by super-positioning the results from each position  $z_c$ .

The transmitting signal is a continuous wave (CW) signal with a frequency of  $f_0$  modulated with an m-sequence of chip width  $t_C$ , which gives a range resolution of  $\Delta R = ct_C/2$  [19], [20], where  $c$  is the speed of light. The radar repeats transmissions with an inter-pulse period of  $T_s$ . Here, we define two time variables:  $\tau$  corresponding to the time of echo reception associated with range  $R$ , and  $t$  corresponding to the time of transmission. The received signal at each  $t$  is acquired by taking a cross correlation of a raw received signal with a time-shifted m-sequence [19]. The received signal

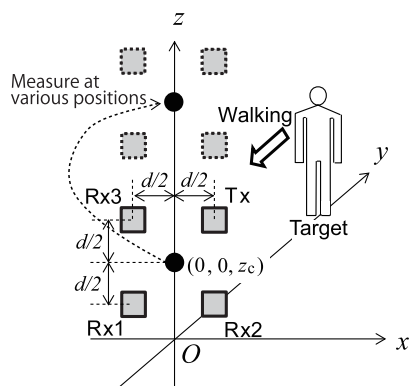


Fig. 1 Schematic of setup for UWB Doppler radar.

$s_i(\tau)$  using receiver  $i$  after the cross correlation and demodulation processes is expressed as:

$$s_i(\tau) = \sum_n A_{Rn} r_T(\tau - \tau_{pn}) e^{j2\pi f_{dn}(\tau - \tau_{pn})}, \quad (1)$$

where  $r_T(\tau)$  is the autocorrelation of the transmitting m-sequence,  $\tau_{pn}$  is the time delay corresponding to the distance between Rx<sub>i</sub> and the  $n$ -th target,  $A_{Rn}$  is the receiving amplitude corresponding to the  $n$ -th target, and  $f_{dn}$  is the Doppler frequency of the  $n$ -th target. We acquire a received signal  $s_{ik}(t)$  for each range bin  $k$  by discretizing  $s_i(\tau)$  in terms of the time delay for all  $t$ . The time delay after the discretization corresponding to range bin  $k$  is expressed as  $\tau_{pk} = 2k\Delta R/c$ .

### 2.2 Imaging Procedure

The UWB Doppler radar imager separates multiple scattering centers in the time-frequency distribution and estimates the positions of the extracted scattering centers [15], [16]. If different scattering centers have different radial velocities, we can separate these using the differences in their Doppler frequencies. The Doppler frequency is expressed as:

$$f_d = \frac{2v_d}{\lambda}, \quad (2)$$

where  $v_d$  is the radial velocity and  $\lambda$  is the wavelength. The radial velocity  $v_d$  of each time is determined by time-frequency analysis of the received signals. Time-frequency distribution  $S_{ik}(t, v_d)$  in this study was obtained by using a sliding-window discrete Fourier transform (SDFT) [21] of  $s_{ik}(t)$ .  $S_{ik}(t, v_d)$  is calculated by:

$$S_{ik}(t, v_d) = \int_{-\infty}^{\infty} s_{ik}(v) w_H(v - t) e^{-j4\pi v_d v / \lambda} dv, \quad (3)$$

where  $j = \sqrt{-1}$  and  $w_H(t)$  is the Hamming window function, which is expressed as:

$$w_H(t) = \begin{cases} 0.54 - 0.46 \cos \frac{2\pi}{T_w} t & (0 \leq t \leq T_w) \\ 0 & (\text{otherwise}), \end{cases} \quad (4)$$

where  $T_w$  is the window size. The SDFT calculates Eq. (3) for all the time bins. We extract the significant peaks of  $S_{ik}(t, v_d)$ , and these peaks correspond to the scattering centers using the following conditions:

$$d|S_{ik}(t, v_d)|/dv_d = 0, \quad (5)$$

$$|S_{ik}(t, v_d)|^2 > \rho \max_{v_d} |S_{ik}(t, v_d)|^2, \quad (6)$$

where  $\rho > 0$  is the ratio of the peak extraction threshold power to the maximum power, and is empirically determined [14].

We then estimate the position of each extracted scattering center. The direction-of-arrival (DOA) is estimated by means of interferometry. The elevation DOA  $\theta_{ELn}$  and azimuth DOA  $\theta_{AZn}$  of the  $n$ -th scattering center are calculated by:

$$\theta_{EL}(t, v_{dn}) = \sin^{-1} \left[ \frac{\angle S_{1k'}(t, v_{dn}) - \angle S_{3k'}(t, v_{dn})}{(2\pi d/\lambda)} \right], \quad (7)$$

$$\theta_{AZ}(t, v_{dn}) = \sin^{-1} \left[ \frac{\angle S_{1k'}(t, v_{dn}) - \angle S_{2k'}(t, v_{dn})}{\{2\pi d \cos \theta_{EL}(t, v_{dn})/\lambda\}} \right], \quad (8)$$

where  $k'$  is the range bin where the  $n$ -th target is detected. Distance is estimated by finding the range that maximizes the echo intensity using the range interpolation method [14], [15]. The distance  $R_1(t, v_{dn})$  with the range resolution  $\Delta R$  is estimated by finding the range that maximizes the echo intensity as:

$$R_1(t, v_{dn}) = \Delta R \arg \max_k |S_{1k}(t, v_{dn})|. \quad (9)$$

To acquire the distance to an accuracy better than  $\Delta R$ , the range interpolation is applied with the calibration function  $D(P_1/P_2)$ . Here,  $P_1$  is the maximum power of the received signal,  $P_2$  is the power of the adjacent range sample, and  $D(P_1/P_2)$  expresses the relationship between the ratio of these and the fractional range. We determine  $D(P_1/P_2)$  by the calibration experiment [14] in advance, and the accurate distance  $R(t, v_{dn})$  is estimated by:

$$R(t, v_{dn}) = R_1(t, v_{dn}) + D(P_1/P_2). \quad (10)$$

The positions of scattering centers  $\mathbf{x}_s(t, v_{dn})$  are determined by:

$$\mathbf{x}_s(t, v_{dn}) = \begin{bmatrix} x_s(t, v_{dn}) \\ y_s(t, v_{dn}) \\ z_s(t, v_{dn}) \end{bmatrix} = \begin{bmatrix} R(t, v_{dn}) \cos \theta_{EL}(t, v_{dn}) \sin \theta_{AZ}(t, v_{dn}) \\ R(t, v_{dn}) \cos \theta_{EL}(t, v_{dn}) \cos \theta_{AZ}(t, v_{dn}) \\ R(t, v_{dn}) \sin \theta_{EL}(t, v_{dn}) + z_c \end{bmatrix}. \quad (11)$$

In addition, we apply a method of rejecting false images [16] to estimate  $\mathbf{x}_s(t, v_{dn})$  to reduce the effect of interference between multiple scattering centers. In this method we delete the points that satisfy the following equations:

$$d\mathbf{x}_s(t, v_{dn})/dt > v_{\max}, \quad (12)$$

and

$$N_{\mathbf{x}_s(t, v_{dn})}/N_A < n_{th}, \quad (13)$$

where  $v_{\max}$  is the assumed maximum velocity,  $N_{\mathbf{x}_s(t, v_{dn})}$  is the number of estimated scattering centers within a sphere whose center is  $\mathbf{x}_s(t, v_{dn})$  and radius is  $R_F$ . The number  $n_{th}$  is the threshold ratio of the number of points to the number of estimated scattering centers  $N_A$ . Parameters  $v_{\max}$ ,  $R_F$ , and  $n_{th}$  are empirically determined taking into consideration target motion and spatial resolution.

### 3. Imaging of Various Types of Pedestrians

This section presents examples of imaging various types of pedestrians in the experiment, and discusses the features of each image. Figure 2 has photographs of the types of pedestrians we assumed. This study took into account the classification of three groups and six types of pedestrians. We assumed three groups of pedestrians: targets in group A were walking targets with normal leg motion, targets in group B were pedestrians with a three-point crutch swinging gait, and targets in group C were moving in wheelchairs. Moreover, target group A had three walking styles: target A-a was a normal pedestrian who swung his arms (corresponding to FAM), target A-b carried a bag in one hand (corresponding to PAM), and target A-c walked with his hands in his pockets (corresponding to NAM). Target group C had two target types: target C-a was a pedestrian pushing a person in a wheelchair, and target C-b was a person propelling himself in a wheelchair. All targets walked from  $(x, y) = (0, 3.9 \text{ m})$  to  $(0, 1.5 \text{ m})$ . The mean speeds of target groups A, B, and C were 0.8, 0.76 and 0.7 m/s, and they walked at an approximately constant speed.

The radar parameters were  $d=3.5 \text{ cm}$ ,  $f_0=26.4 \text{ GHz}$ ,  $T_s=1.29 \text{ ms}$  and  $t_c=2 \text{ ns}$  which corresponded to  $\Delta R=30 \text{ cm}$ . The window size for the SDFT was 165 ms. Horn antennas were used with a  $-3 \text{ dB}$  beamwidth of  $\pm 11^\circ$  on both the E- and H-planes. This beamwidth is not sufficient to acquire data that corresponds to the whole body. To estimate the image of the whole body, we iterated measurements four times for each pedestrian target whose gait cycle and walking step

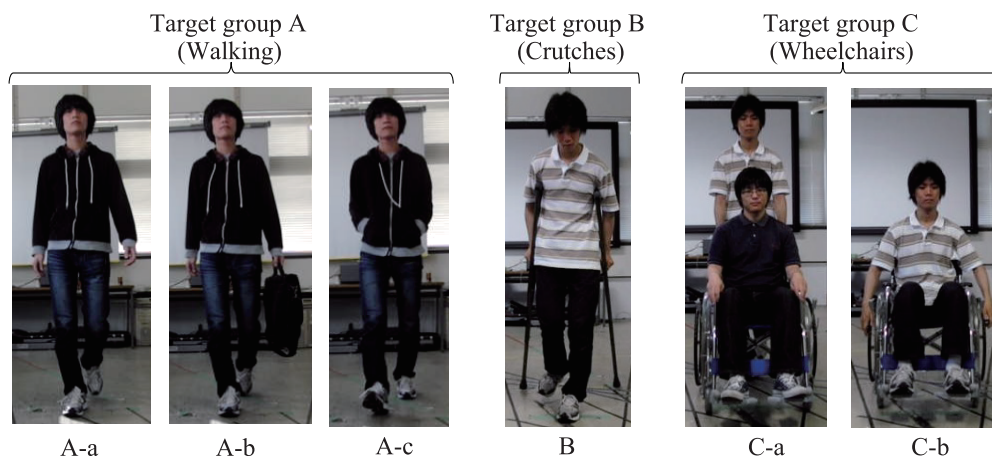
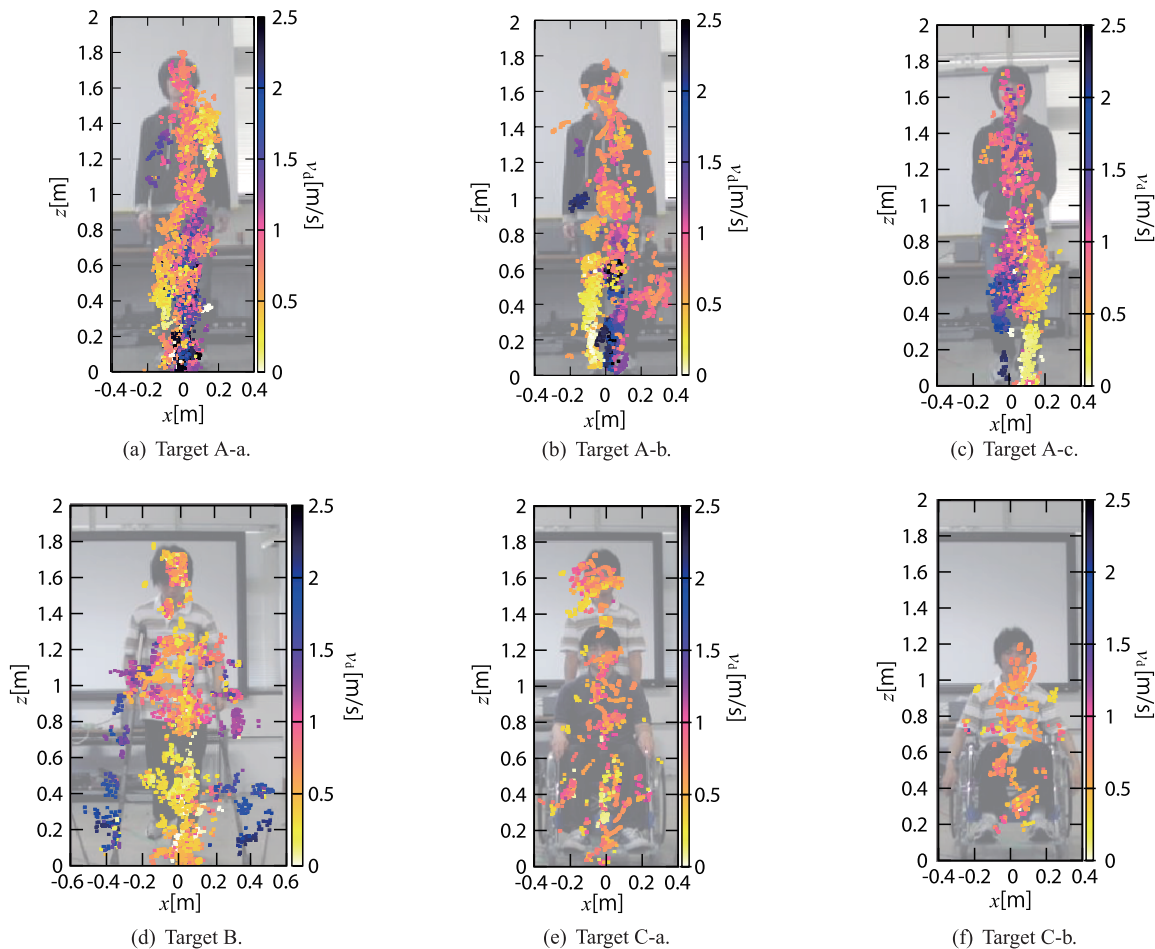


Fig. 2 Assumed pedestrian types.



**Fig. 3** Frontal views of images estimated using the method of UWB Doppler radar imaging.

were fixed, and set different  $z_c$  in each measurement. In this paper, we took measurements at  $z_c = 0.36, 0.83, 1.3,$  and  $1.5$  m. Note that this antenna scanning process is not required when wide-directivity antennas are used. The parameters for the method of UWB Doppler imaging were  $\rho = 0.15$ ,  $v_{\max} = 2.5$  m/s,  $R_F = \Delta R/10 = 3$  cm, and  $n_{\text{th}} = 1/400$ . We used data corresponding to one cycle of a time-frequency distribution (corresponding to half the walking cycle) for imaging and classification. The data collection time for each target and antenna position was 0.7–0.8 s.

Figure 3 shows the frontal views of the estimated images for all pedestrian types. As we can see from Fig. 3(a), there is an outline of the human shape. Moreover, we can recognize from radial velocity information that the left leg and the right arm have forward motion in this half of the walking cycle. Although target A-b has nearly the same properties as target A-a, the number of scattering centers corresponding to arms is relatively small as seen in Fig. 3(b). This is because his arm-swing amplitude is limited because of PAM. We can observe the scattering centers on the bag at approximately  $(x, z) = (0.25 \text{ m}, 0.5 \text{ m})$ , as shown in Fig. 3(b). Figure 3(c) indicates that scattering centers corresponding to arms have not been acquired. This is because the peaks corresponding to the arms were not detected in the time-

frequency distribution because of NAM. We confirmed the images of crutches and their relatively high velocities that corresponded to their forward motion as seen in Fig. 3(d). Figure 3(e) shows the scattering centers are concentrated in a relatively narrow region in terms of both position and  $v_d$ , because the wheelchair was moving toward the radar at an approximately constant velocity. The same feature can also be confirmed in target C-b. Moreover, we can confirm scattering centers that slightly correspond to arm motion from Fig. 3(f) at approximately  $(x, z) = (-0.2 \text{ m}, 0.75 \text{ m})$ , and the image is shorter than those of the other types. These results indicate that the method of UWB Doppler radar imaging extracts various characteristics of pedestrians, and the features of each pedestrian can be confirmed from the estimated images and  $v_d$  information.

## 4. Extraction of Feature Parameters

### 4.1 Extraction of Silhouettes from Frontal Images

We propose feature parameters to classify pedestrians in this section. The proposed feature parameters are extracted from the silhouettes and radial velocity distributions of the estimated images. First, we extract the shape of an image

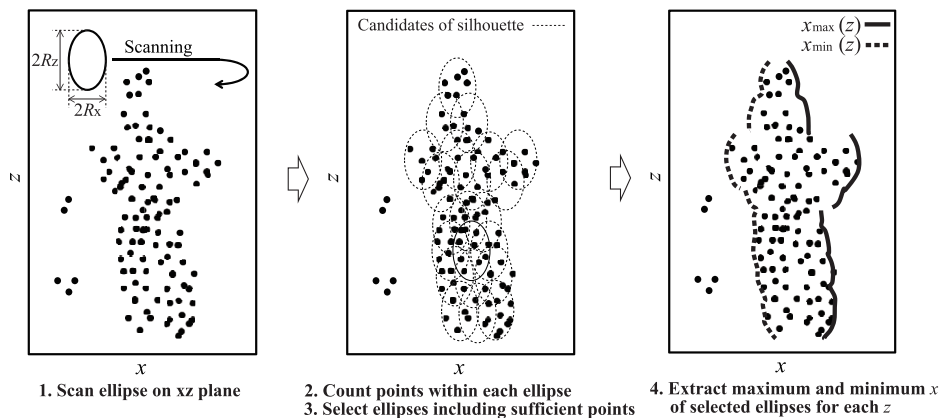


**Fig. 4** Outline of the method to extract silhouettes.

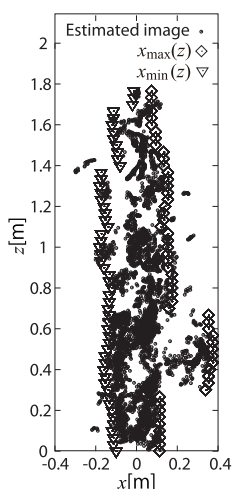


**Fig. 5** Extracted silhouette of the image in Fig. 3(b).

silhouette. For example, the most important difference between target C-b and the others is the height of the image, and this is estimated as the silhouette's height. Figure 4 outlines the method we propose for extracting silhouettes, which can be explained in four steps:

1. Scan an ellipse whose major axis is parallel to the  $z$ -axis and minor axis is parallel to the  $x$ -axis on the  $xz$  plane. The length of the major and minor axes are defined as  $R_z$  and  $R_x$ .
2. Count the number of estimated scattering centers  $N_s(x_{ec}, z_{ec})$  within each ellipse whose central position is  $(x_{ec}, z_{ec})$ .
3. If  $N_s(x_{ec}, z_{ec}) > \gamma N_A$ , points on the ellipse  $(x_e, z_e)$  are candidates for the silhouette, where  $\gamma$  is the threshold ratio of  $N_s$  to the number of total estimated points  $N_A$ .
4. Extract the maximum and minimum  $x_e$  from the candidate points for each  $z_e$ , and these silhouette points are defined as  $x_{\max}(z)$  and  $x_{\min}(z)$  ( $z_{\max} < z < z_{\min}$ ), where  $z_{\max}$  and  $z_{\min}$  are the maximum and minimum of  $z_e$ .

Figure 5 shows the estimated image silhouette of Fig. 3(b). We empirically set  $R_x=2$  cm,  $R_z=10$  cm, and

$\gamma=0.004$ . The silhouette of the image is extracted as can be seen from this figure.

We then extract the parameters for the silhouette shapes. First, the height of the silhouette is extracted as:

$$H_S = z_{\max} - z_{\min}. \quad (14)$$

Next, we extract the width and center of the silhouette in the high and low  $z$  regions. These are used to extract the parameters of the radial velocity features, which is described in the next section. We extract the mean width of the silhouette in the high  $z$  region as:

$$W_H = E[x_{\max}(z) - x_{\min}(z) | z > \alpha_H H_S], \quad (15)$$

where  $E[X | C_1, C_2, \dots]$  means the average of  $X$  that satisfies conditions  $C_1, C_2, \dots$ , and  $\alpha_H < 1$  is a threshold ratio of  $z$  to height  $H_S$ . A mean center in terms of  $x$  in the high  $z$  region is estimated as:

$$x_{cH} = E[(x_{\max}(z) + x_{\min}(z))/2 | z > \alpha_H H_S]. \quad (16)$$

Moreover, we extract  $W_L$  and  $x_{cL}$ , which is determined in the same way by using the silhouette that satisfies  $z < \alpha_L H_S$ .

#### 4.2 Parameters of the Radial Velocity Distribution in Each Region of the Image

We propose feature parameters based on the radial velocity features of the estimated images in this subsection. First, we examine radial velocity distributions in the relatively low  $z$  region to classify target groups A, B, and C. Figure 6(a) shows the radial velocity distributions of the estimated images in Figs. 3(a), (d), and (e) for  $z < 0.4H_S$ . Targets A-a and B have a radial velocity spread that corresponds to the forward motion of legs or crutches. In contrast, the radial velocity spread of target C-a is small because of the constant speed of the wheelchair. Thus, the standard deviation of the radial velocity distribution can be effectively used to classify target groups C and A or B. The standard deviation of the radial velocity distribution in the low  $z$  region is determined by:

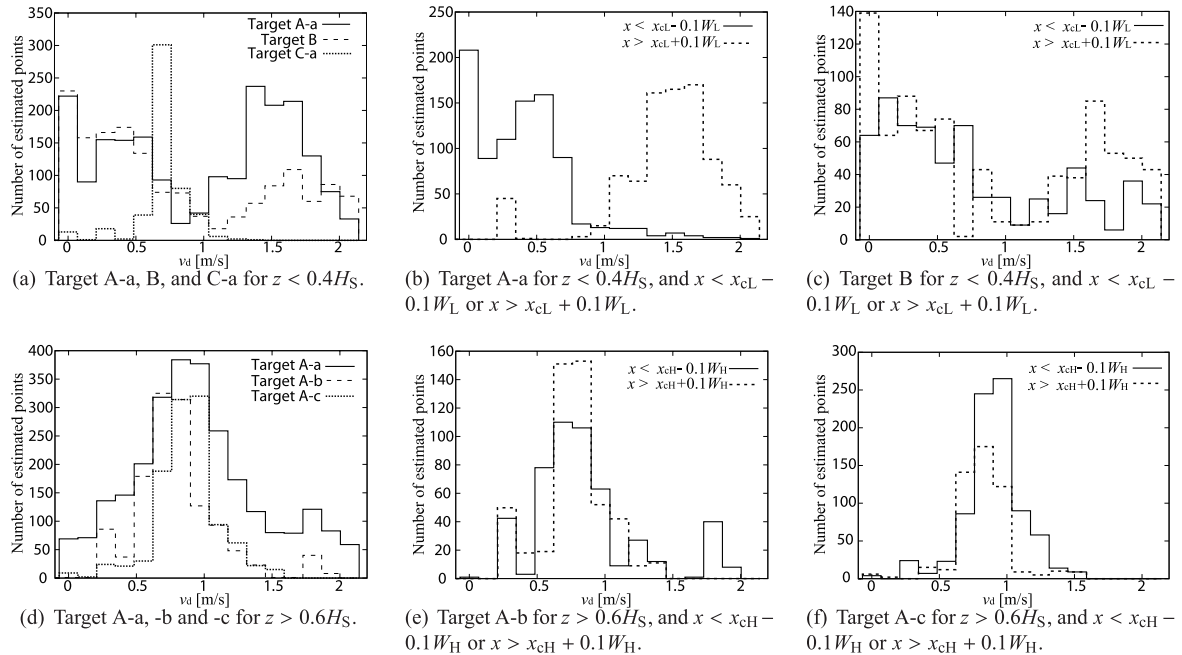


**Fig. 6** Radial velocity distributions of the estimated images shown in Fig. 3 for the various regions.

$$\sigma_L = \text{Std}[v_d | z_s < \alpha_L H_S], \quad (17)$$

where  $\text{Std}[X | C_1, C_2, \dots]$  is the standard deviation determined by  $\{\text{E}[X^2 | C_1, C_2, \dots] - (\text{E}[X | C_1, C_2, \dots])^2\}^{1/2}$ . Next, we consider the classification of target groups A and B. As seen in Fig. 3(d), target group B has an approximately symmetrical distribution with respect to the  $z$ -axis near the floor. In contrast, the targets in group A have asymmetric distributions on the  $z$ -axis corresponding to the asymmetrical motion of legs in half a walking cycle. Figures 6(b) and (c) show the radial velocity distributions in Figs. 3(a) and (d) for  $z < 0.4H_S$  and  $x < x_{cL} - 0.1W_L$  or  $x > x_{cL} + 0.1W_L$ . The region near the  $x_{cH}$  is excluded because the properties of the left and right sides of the estimated image are mixed. As we can see from these figures, there is a difference between the averages of both distributions for target A-a, while target group B shows no difference between the distributions of both regions. Thus, we use the average difference for both regions, which is expressed as:

$$\Delta\mu_L = | \text{E}[v_d | x_s > x_{cL} + \beta W_L, z_s < \alpha_L H_S] - \text{E}[v_d | x_s < x_{cL} - \beta W_L, z_s < \alpha_L H_S] |, \quad (18)$$

where  $\beta < 1$  is the threshold ratio of  $x$  to the mean width of the silhouette.

Next, we discuss the classification of gait types in target group A. The difference in arm movements in Figs. 3(a), (b), and (c) is detected from estimated images that correspond to the upper parts of the body. Figure 6(d) shows the radial velocity distributions in Figs. 3(a), (b), and (c) for  $z > 0.6H_S$ . As we can see from this figure, the standard deviation of the radial velocity in the high  $z$  region is an effective parameter, which is estimated as:

$$\sigma_H = \text{Std}[v_d | z_s > \alpha_H H_S]. \quad (19)$$

The asymmetry between motion in the left and right arms is an important feature of target A-b. Figures 6(e) and (f) show the radial velocity distributions for  $z > 0.6H_S$  and  $x < x_{cH} - 0.1W_H$  or  $x > x_{cH} + 0.1W_H$ . Similar to Eq. (18), the difference in the average in the high  $z$  region is expressed as:

$$\Delta\mu_H = | \text{E}[v_d | x_s > x_{cH} + \beta W_H, z_s > \alpha_H H_S] - \text{E}[v_d | x_s < x_{cH} - \beta W_H, z_s > \alpha_H H_S] |. \quad (20)$$

In addition, there is a difference in the standard deviation of both regions in target A-b, which is extracted by:

$$\Delta\sigma_H = | \text{Std}[v_d | x_s > x_{cH} + \beta W_H, z_s > \alpha_H H_S] - \text{Std}[v_d | x_s < x_{cH} - \beta W_H, z_s > \alpha_H H_S] |. \quad (21)$$

Targets A-a, -b, and -c are classified using these parameters. Moreover, the target C-b and others are classified using the height  $H_S$ . Based on the above, we propose a feature vector that is expressed as:

$$\psi = (\sigma_L, \Delta\mu_L, \sigma_H, \Delta\mu_H, \Delta\sigma_H, H_S). \quad (22)$$

## 5. Classification Using the $k$ -Nearest Neighbor Algorithm

We classified targets using the proposed feature vector extracted from the experimental results, which is explained in this section. We also explain the classification procedure. In this section, we derive one pedestrian type from the six types of pedestrians described in Sect. 3, and evaluate the degree of accuracy from the viewpoint of the three groups and six types of classification. The experimental setup and parameters were the same as those in Sect. 3. The parameters for the process to extract the silhouettes were the same

**Table 1** Parameters of subjects.

Subject number	Height [m]	Mean speed [m/s]	Number of data for each pedestrian type
(i)	1.75	0.83	20
(ii)	1.72	0.78	15
(iii)	1.70	0.86	15
(iv)	1.63	0.74	20

**Table 2** Mean values of proposed feature parameters.

	$\sigma_L$	$\Delta\mu_L$	$\sigma_H$	$\Delta\mu_H$	$\Delta\sigma_H$	$H_S$
A-a	0.489	0.643	0.357	0.407	0.0912	1.69
A-b	0.486	0.530	0.238	0.179	0.184	1.70
A-c	0.491	0.677	0.175	0.0736	0.0408	1.69
B	0.489	0.138	0.218	0.0820	0.0507	1.67
C-a	0.127	0.0590	0.108	0.0508	0.0334	1.67
C-b	0.104	0.0518	0.116	0.0557	0.0449	1.16

**Table 3** Confusion matrix. AT represents the actual type, and ET represents the type estimated using the 3-NN algorithm.

AT \ ET	A-a	A-b	A-c	B	C-a	C-b
A-a	46	4	0	0	0	0
A-b	3	44	3	0	0	0
A-c	0	0	49	1	0	0
B	0	0	0	50	0	0
C-a	0	0	0	1	49	0
C-b	0	0	0	0	0	50

as those in Sect. 4.1. The threshold parameters for radial velocity distributions  $\alpha_L$ ,  $\alpha_H$ , and  $\beta$  were empirically determined as 0.4, 0.6, and 0.1. We assumed four subjects, and their parameters are listed in Table 1. Table 2 summarizes the mean values of the parameters estimated from the data for these subjects. We can see clear differences between the types of pedestrians.

The types of pedestrians with extracted feature parameters were classified using the  $k$ -NN algorithm, which classifies objects based on the closest examples for training purposes [17]. The procedure for classification involves three steps:

1. Prepare the training data set,  $\psi_{tr}$ .
2. Calculate the Euclidean distance between an unlabeled feature vector,  $\psi$ , and all  $\psi_{tr}$ .
3. Classify  $\psi$  to the label which most frequently appears in  $k$  training vectors nearest to  $\psi$ .

We set the data of subject (i) to  $\psi_{tr}$ , and  $k=3$ . The setting of  $k$  and the determination of the number of training data are discussed in the next section. Table 3 summarizes the confusion matrix for the classification results for subjects (ii)–(iv). Although there is slight misclassification of targets A-a, -b, and -c, accurate classification is generally achieved. The degree of classification accuracy for the six types is 96.0%. Moreover, the degree of classification accuracy is 99.3% with respect to the classification of the three groups. The input time duration for each set of data is less than 0.8 s, and the average of the total calculation time for the imaging and classification processes is 0.55 s using an Intel Core 2 Duo 3.33-GHz processor. These results mean that our proposed

feature parameters and classification procedures could accurately classify pedestrians in real time. In real use, however, the classification system has to derive one pedestrian type from whole situations including non-pedestrian targets. The degree of classification accuracy of 96.0% does not consider these situations. Section 6.3 examines some of these alternative situations.

## 6. Discussion

### 6.1 Evaluation of Performance for the Quantity of Training Data and Comparison with SVM

This subsection discusses our investigations into the performance of our proposed method of classification with respect to the quantity of training data. Moreover, we compared the  $k$ -NN algorithm with a support vector machine (SVM), which is another effective algorithm for discrimination analysis [22], [23]. This section uses a soft-margin multi-class SVM with a Gaussian kernel function [23]. We investigated the degree of classification accuracy using the 1- and 3-NN algorithms and an SVM for the ratio of the quantity of training data to all data. The experimental setting, parameters, and the data used were the same as those presented in the previous section, and the training data set was randomly selected.

Figures 7 and 8 plot the relationships between the degree of classification accuracy and the quantity of training data to classify the six types and three groups, where  $N_{train}$  and  $N_{all}$  correspond to the quantity of training and all data. As seen in these figures, the  $k$ -NN algorithms classify more accurately than the SVM, and the 3-NN is better than 1-NN when the quantity of training data is relatively large. The 3-NN algorithm achieves 99% accuracy in classifying the three groups when  $N_{train}/N_{all}$  is larger than 15%, and 95% accuracy in classifying the six types when  $N_{train}/N_{all}$  is greater than 20%. These results mean that the 3-NN algorithm can classify pedestrian targets accurately with a relatively small quantity of training data.

### 6.2 Assessment of Suitable Parameters

This subsection discusses the parameters used with our proposed method. First, we explain the setting of the spatial threshold parameters  $\alpha_L$ ,  $\alpha_H$ , and  $\beta$ . Here, we present  $\Delta\mu_L$  of targets A-a and B for each  $\alpha_L$  as an example. Figure 9 plots the relationship between  $\alpha_L$  and the mean value of  $\Delta\mu_L$ . The difference between the target types is relatively large for  $0.25 < \alpha_L < 0.5$ . Other parameters can be set similarly. Therefore, we can easily choose appropriate parameters based on a few examples.

We now discuss the  $k$  of the  $k$ -NN algorithm. Figure 10 plots the relationship between  $k$  and the degree of classification accuracy for the six types. The values of  $k = 1$  or 3 were better. In addition,  $k = 3$  was better when there was a relatively large quantity of training data. The accuracy deteriorated when  $k$  was an even number because the

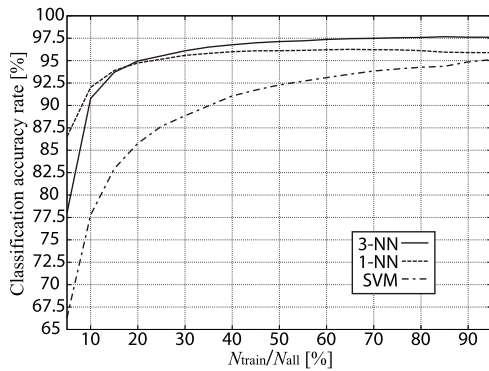


Fig. 7 Degree of classification accuracy for the six types versus quantity of training data.

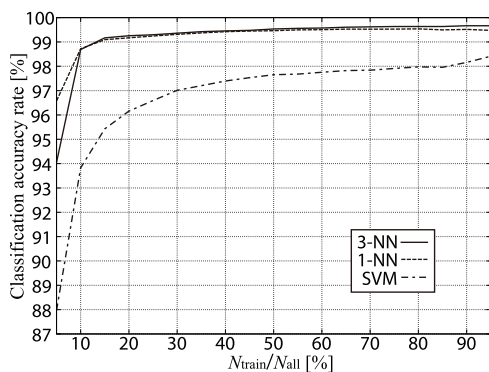


Fig. 8 Degree of classification accuracy for the three groups versus quantity of training data.

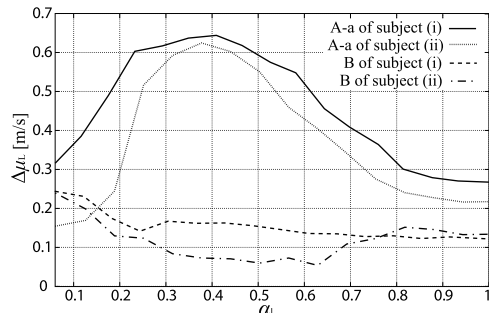


Fig. 9 Relationships between  $\alpha_L$  and  $\Delta\mu_L$  for targets A-a and B.

$k$ -NN algorithm randomly selected a label when there was the same number of classes.

### 6.3 Discussion on the Variety of Motions

Finally, we discuss the possibility of classifying other types of targets such as a person carrying a box on a hand cart, a short person, and a person making other movements. The main characteristic of a target pushing a hand cart was almost the same as for target C-a, and the classification of normal pedestrians and those on crutches was possible using  $\sigma_L$  and  $\sigma_H$ . Although target C-b and others could be classified with  $H_S$ , it was difficult to classify a short person

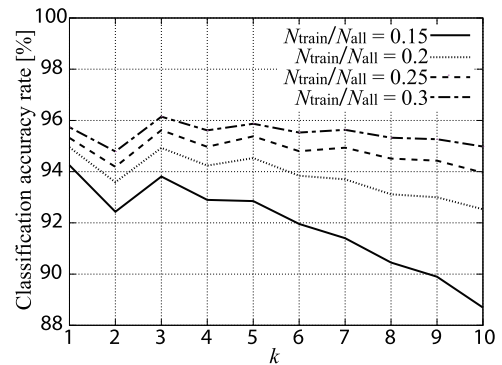


Fig. 10 Relationship between  $k$  and the degree of classification accuracy.

such as a child with only this parameter. However, if the short person made leg or arm movements, classification using  $\sigma_L$  and  $\sigma_H$  was possible. Furthermore, it was possible to classify a variety of motion types (e.g. running, sitting, rotating, and jumping [6], [13]). We can easily predict that the differences in these motion types will be clearly extracted as velocity and silhouette parameters.

## 7. Conclusions

This paper presents an accurate method for classifying pedestrians in real time. We first demonstrated that accurate imaging could be accomplished with a UWB Doppler radar for a variety of pedestrian targets, and discussed the features of each target. We then proposed effective feature parameters based on UWB Doppler radar images and their radial velocity features. The experiments took into consideration six types of pedestrians (those with FAM, PAM, and NAM, those on crutches and in wheelchairs, and a person propelling himself in a wheelchair) and we found that they were classified with an accuracy of 96% using the  $k$ -NN algorithm. The total calculation time for the imaging and classification processes was 0.55 s. In addition, an accuracy of 99% was accomplished in classifying the three groups (normal pedestrians, those on crutches and both wheelchair groups). Finally, we clarified how well the method performed, found suitable parameter settings for the proposed algorithm, and discussed its capabilities in classifying other types of targets. However, the proposed method assumed only a single person walking towards the radar. Our other studies showed applications to a pedestrian moving in diagonal directions [14] and two closely spaced pedestrians [24]. Thus, important future research is to extend to other situations based on these studies.

## Acknowledgments

This work was supported in part by a Grant-in-Aid for Scientific Research (A) (Grant No. 21246065) and a Grant-in-Aid for JSPS Fellows (Grant No. 246485).

## References

- [1] A. Dhital, P. Closas, and C. Fernández-Prades, "Bayesian filtering for indoor localization and tracking in wireless sensor networks," *EURASIP J. Wirel. Commun. Netw.*, Article Number 21, 2012.
- [2] S. Hantscher, B. Schlenker, M. Hagelen, S.A. Lang, H. Essen, A. Tessmann, A. Hulsmann, A. Leuther, and M. Schlechtweg, "Security pre-screening of moving persons using a rotating multichannel W-Band radar," *IEEE Trans. Micro. Theo. Tech.*, vol.60, no.3, pp.870–880, 2012.
- [3] Y. Wang and A.E. Fathy, "Advanced system level simulation platform for three-dimensional UWB through-wall imaging SAR using time-domain approach," *IEEE Trans. Geosci. Remote Sens.*, vol.50, no.5, pp.1986–2000, 2012.
- [4] H. Hatano, K. Sugiyama, T. Mizutani, and Y. Kuwahara, "Error reduction algorithm for target position estimation using reflected signals," *IEICE Trans. Commun.*, vol.E94-B, no.10, pp.2886–2890, Oct. 2011.
- [5] X. Zhuge and A.G. Yarovoy, "A sparse aperture MIMO-SAR-based UWB imaging system for concealed weapon detection," *IEEE Trans. Geosci. Remote Sens.*, vol.49, no.1, pp.509–517, 2011.
- [6] Y. Kim and H. Ling, "Human activity classification based on micro-Doppler signatures using a support vector machine," *IEEE Trans. Geosci. Remote Sens.*, vol.47, no.5, pp.1328–1337, 2009.
- [7] I. Orović, S. Stanković, and M. Amin, "A new approach for classification of human gait based on time-frequency feature representations," *Signal Processing*, vol.91, no.6, pp.1448–1456, 2011.
- [8] F.H.C. Tivive, A. Bouzerdoum, M. Herberthson, and M.G. Amin, "A human gait classification method based on radar Doppler spectrogram," *EURASIP J. Adv. Sig. Proc.*, vol.2010, Article ID 389716, 2010.
- [9] A. Sume, M. Gustafsson, M. Herberthson, A. Jänis, S. Nilsson, J. Rham, and A. Örbom "Radar detection of moving targets behind corners," *IEEE Trans. Geosci. Remote Sens.*, vol.49, no.6, pp.2259–2267, 2011.
- [10] P. Setlur, F. Ahmad, and M. Amin, "Maximum likelihood and sub-optimal schemes for micro-Doppler estimation using carrier diverse Doppler radars," *Inst. Eng. Tech. Signal Processing*, vol.5, no.2, pp.194–208, 2011.
- [11] D.P. Fairchild and R.M. Narayanan, "Human activity classification using Hilbert-Huang transform analysis of radar Doppler data," *Proc. Society of Photo-Optical Instrumentation Engineers (SPIE) 8021, Florida, USA, 80210F*, 2011.
- [12] T. Thayaparan, S. Abrol, E. Riseborough, L. Stankovic, D. Lamothe, and G. Duff, "Analysis of radar micro-Doppler signatures from experimental helicopter and human data," *IET Radar Sonar Navig.*, vol.1, no.4, pp.289–299, 2007.
- [13] J.D. Bryan, J. Kwon, N. Lee, and Y. Kim, "Application of ultra-wide band radar for classification of human activities," *IET Radar Sonar Navig.*, vol.6, no.3, pp.172–179, 2012.
- [14] K. Saho, T. Sakamoto, T. Sato, K. Inoue, and T. Fukuda, "Pedestrian imaging using UWB Doppler radar interferometry," *IEICE Trans. Commun.*, vol.E96-B, no.2, pp.613–623, Feb. 2013.
- [15] K. Saho, T. Sakamoto, T. Sato, K. Inoue, and T. Fukuda, "High-resolution UWB Doppler radar interferometric imaging algorithm for multiple moving targets with smoothed pseudo Wigner distribution," *IEICE Technical Report*, vol.110, no.250, pp.261–266, 2010.
- [16] K. Saho, T. Sakamoto, T. Sato, K. Inoue, and T. Fukuda, "Experimental study of real-time human imaging using UWB Doppler radar interferometry," *Proc. 6th European Conf. Antennas and Propagation (EuCAP2012), Prague, Czech Republic*, pp.3495–3499, 2012.
- [17] T.M. Cover and P.E. Hart, "Nearest neighbor pattern classification," *IEEE Trans. Inf. Theory*, vol.13, pp.21–27, 1968.
- [18] Y. Liao and V.R. Vemuri, "Use of K-nearest neighbor classifier for intrusion detection," *Computers Security*, vol.21, no.5, pp.439–448, 2002.
- [19] R. Pickholts, D. Schilling, and L.B. Milstein, "Theory of spread-spectrum communications-A tutorial," *IEEE Trans. Commun.*, vol.COM-30, pp.855–882, 1982.
- [20] T. Fukuda, N. Nagoro, S. Ujita, S. Nagai, M. Nishijima, H. Sakai, T. Tanaka, and D. Ueda, "A 26 GHz short-range UWB vehicular radar using 2.5 Gcps spread spectrum modulation," *IEEE/MTT-S Int. Microwave Symp. 2007*, pp.1311–1314, 2007.
- [21] E. Jacobsen and R. Lyons, "The sliding DFT," *IEEE Trans. Signal Process. Mag.*, vol.20, no.2, pp.74–80, 2003.
- [22] C.J.C. Burges, "A tutorial on support vector machines for pattern recognition," *Data Mining and Knowledge Discovery*, vol.2, no.2, pp.121–167, 1998.
- [23] C.W. Hsu and C.J. Lin, "A comparison of methods for multiclass support vector machines," *IEEE Trans. Neural Netw.*, vol.13, no.2, pp.415–425, 2002.
- [24] H. Homma, K. Saho, T. Sakamoto, T. Sato, K. Inoue, and T. Fukuda, "Accurate image separation of pedestrians with UWB Doppler imaging radars," *IEICE Technical Report*, vol.111, no.407, pp.67–72, 2012. (in Japanese)



**Kenshi Saho** received his B.E. degree from Kyoto University in 2008 and M.I. and Ph.D. degrees from the Graduate School of Informatics, Kyoto University, in 2010 and 2013, respectively. He is currently a Research Fellow of the Japan Society for the Promotion of Science (JSPS) with the Department of Communications and Computer Engineering, Graduate School of Informatics, Kyoto University. His current research interest is in signal processing and pattern recognition for UWB radars. He is a member

of the IEEEJ.



**Takuya Sakamoto** received his B.E. degree from Kyoto University in 2000, and M.I. and Ph.D. degrees from the Graduate School of Informatics, Kyoto University in 2002 and 2005, respectively. He is an assistant professor in the Department of Communications and Computer Engineering, Graduate School of Informatics, Kyoto University. His current research interest is in UWB radar signal processing. He is a member of the IEEEJ and the IEEE.



**Toru Sato** received his B.E., M.E., and Ph.D. degrees in electrical engineering from Kyoto University, Kyoto, Japan in 1976, 1978, and 1982, respectively. He has been with Kyoto University since 1983 and is currently a Professor in the Department of Communications and Computer Engineering, Graduate School of Informatics. His major research interests include system design and signal processing aspects of UWB radars, atmospheric radars, radar remote sensing of the atmosphere, and radar observation

of space debris. He is a member of the Institute of Electrical and Electronics Engineers, the Society of Geomagnetism and Earth, Planetary and Space Sciences, the Japan Society for Aeronautical and Space Sciences, and American Meteorological Society.



**Kenichi Inoue** received the B.S. and M.S. degrees in electronic science and engineering from Kyoto University, Kyoto, Japan, in 2000 and 2002, respectively. In 2002, he joined Semiconductor Device Research Center, Semiconductor Company, Matsushita Electric Industrial Co. Ltd., Osaka, Japan, where he was working on semiconductor laser devices, sensor devices and sensor systems. Since 2009, he has been with Advanced Technology Research Laboratories, Panasonic Corporation, Kyoto, Japan,

where he is involved in the research and development of UWB radar sensor system and its applications. Mr. Inoue is a member of the Japan Society of Applied Physics and the Institute of Electronics, Information and Communication Engineers of Japan.



**Takeshi Fukuda** was born in Osaka, Japan, in 1969. He received the B.S. and M.S. degrees in Electronic Engineering from Osaka University, Suita, Japan, in 1993 and 1995, respectively. In 1995, he joined the Electronics Research Laboratory, Matsushita Electronics Corporation, Osaka, Japan, where he has been engaged in the research and development of microwave integrated circuits. Since 2009, he has been with Advanced Technology Research Laboratories, Panasonic Corporation, Kyoto, Japan.

His current research interests are algorithms and RF architectures for high-resolution millimeter-wave radar systems.